ADVANCES IN ATMOSPHERIC SCIENCES, VOL. 32, MARCH 2015, 389–400

Dominant Cloud Microphysical Processes of a Torrential Rainfall Event in Sichuan, China

HUANG Yongjie[1,2] and CUI Xiaopeng*[1,3]

[1] *Key Laboratory of Cloud-Precipitation Physics and Severe Storms, Institute of Atmospheric Physics, Chinese Academy of Sciences, Beijing* 100029

[2] *University of Chinese Academy of Sciences, Beijing* 100049

[3] *Collaborative Innovation Center on Forecast and Evaluation of Meteorological Disasters, Nanjing University of Information Science & Technology, Nanjing* 210044

(Received 28 March 2014; revised 5 June 2014; accepted 10 July 2014)

ABSTRACT

High-resolution numerical simulation data of a rainstorm triggering debris flow in Sichuan Province of China simulated by the Weather Research and Forecasting (WRF) Model were used to study the dominant cloud microphysical processes of the torrential rainfall. The results showed that: (1) In the strong precipitation period, particle sizes of all hydrometeors increased, and mean-mass diameters of graupel increased the most significantly, as compared with those in the weak precipitation period; (2) The terminal velocity of raindrops was the strongest among all hydrometeors, followed by graupel's, which was much smaller than that of raindrops. Differences between various hydrometeors' terminal velocities in the strong precipitation period were larger than those in the weak precipitation period, which favored relative motion, collection interaction and transformation between the particles. Absolute terminal velocity values of raindrops and graupel were significantly greater than those of air upward velocity, and the stronger the precipitation was, the greater the differences between them were; (3) The orders of magnitudes of the various hydrometeors' sources and sinks in the strong precipitation period were larger than those in the weak precipitation period, causing a difference in the intensity of precipitation. Water vapor, cloud water, raindrops, graupel and their exchange processes played a major role in the production of the torrential rainfall, and there were two main processes via which raindrops were generated: abundant water vapor condensed into cloud water and, on the one hand, accretion of cloud water by rain water formed rain water, while on the other hand, accretion of cloud water by graupel formed graupel, and then the melting of graupel formed rain water.

Key words: torrential rainfall, Sichuan, cloud microphysical processes, numerical simulation

Citation: Huang, Y. J., and X. P. Cui, 2015: Dominant cloud microphysical processes of a torrential rainfall event in Sichuan, China. *Adv. Atmos. Sci.*, **32**(3), 389–400, doi: 10.1007/s00376-014-4066-7.

1. Introduction

Orographic torrential rainfall can cause floods, landslides, debris flows and other natural disasters, constituting a great threat to the lives and properties of people, and representing a great challenge to mountain weather forecasters. The Sichuan Basin, with its complex terrain, is located east of the Tibetan Plateau, north of the Yunnan–Guizhou Plateau, and south of the Qinling Heights. It is a storm-prone place, where debris flows, landslides and other secondary geological disasters occur frequently. Following two major earthquakes—Wenchuan earthquake (2008) and Ya'an earthquake (2013)—the situation has worsened because the soil of Sichuan's complex terrain surrounding these earthquake zones has become much looser, meaning frequent torrential rainfall is more likely to lead to debris flows and other disasters. Therefore, understanding the physical processes responsible for the development of orographic torrential rainfall is crucial for the improvement of operational forecasts in this area.

Sawyer (1956) revealed three important factors for orographic rainfall: larger-scale atmospheric circulation; the interaction of the ambient flow by terrain; and cloud microphysical processes. Smith and Barstad (2004) developed a linear steady-state theory for orographic rainfall and derived a linear precipitation model that can represent many complex processes in orographic rainfall using a relatively simple equation (Crochet et al., 2007; Smith and Evans, 2007). However, this linear model cannot include flow blocking, gravity wave breaking, and other non-linear processes, and uses relatively simple microphysics. Compared with this simple linear model, high-resolution mesoscale models, such as the Weather Research and Forecasting (WRF) model, can better reflect nonlinear dynamics, thermodynamics, and de-

* Corresponding author: CUI Xiaopeng
Email: xpcui@mail.iap.ac.cn

tailed microphysical processes in complex orographic rainfall, which has been intensively applied to studies of severe weather and torrential rainfall (Ge et al., 2008; Maussion et al., 2010; Smith et al., 2010; Wang et al., 2011; He and Li, 2013; Wang et al., 2013; Li et al., 2014). Lu et al. (2009) simulated and analyzed several local heavy rainfall events over the western Sichuan Basin during August 2003 using the Advanced Regional Eta-coordinate Model (AREM), and showed that heavy rainfall events over this area are highly sensitive to the initial local water vapor conditions. Chen et al. (2010) explored a method to improve the accuracy of Sichuan torrential rainfall forecasts based on Bayesian decision theory. Chen and Li (2013) used satellite, radar and routine meteorological data to analyze a mesoscale convective system (MCS) and its effects on short-term heavy rainfall in the Sichuan Basin during July 2012. Wang et al. (2013) simulated and analyzed a rainstorm process influenced by the terrain in Sichuan using the WRF model and carried out a diagnostic analysis using dynamical parameters. Li et al. (2014) analyzed observations and a WRF simulation of a rainstorm process that triggered debris flows, and their results indicated that this precipitation process had a short duration, strong intensity and local characteristics, and the heavy rainfall occurred mainly near steep terrain in the Wenchuan–Ya'an earthquake fault zone. Their study (Li et al., 2014) also noted that, under favorable large-scale circulations, the development of a southwest vortex and its interaction with strong wind at the western edge of the subtropical high enhanced the lifting effects of steep terrain and caused heavy rainfall. Because of the combined effects of complex dynamic, thermodynamic and cloud microphysical processes over complex terrain, more accurate quantitative precipitation forecasts (QPFs) remain a huge challenge. Studies on orographic torrential rainfall in Sichuan, in particular, and studies on cloud microphysical processes associated with torrential rainfall have seldom been conducted, although some numerical sensitivity experiments of cloud microphysical parameterization schemes have been carried out (Li and He, 2011; Liao et al., 2012; Ma et al., 2012). Overall, however, a number of open questions remain. For example, what is the key cloud microphysical process for the formation of orographic torrential rainfall? And what are the main raindrop sources for the production of torrential rainfall?

Li et al. (2014) carried out a numerical simulation of a rainstorm in Sichuan using the WRF model. They discussed the role of large-scale circulation evolution and development of the mesoscale system in the emergence of the rainstorm over complex terrain from macroscopic and dynamic perspectives. However, since the formation of a rainstorm is related to both macroscopic dynamic and cloud microphysical processes, as discussed above, it is necessary to also examine the dominant cloud microphysical processes involved in the torrential rainfall event. To address this, we used similar schemes and the same model as Li et al. (2014) to carry out a high-resolution numerical simulation of the orographic rainfall event. However, as an extension to the work of Li et al. (2014), in our study cloud microphysical data were output and analyzed to investigate the above aspect. The numerical simulation and cloud microphysical scheme are briefly described in section 2, the results are presented in section 3, and a summary is given in section 4.

2. Numerical simulation and cloud microphysical scheme

2.1. *Numerical simulation*

A torrential rainfall event in Sichuan Province of China from 1800 UTC 17 August to 0000 UTC 20 August 2010 was simulated using the same WRF model setup as in Li et al. (2014). The simulation was integrated for 54 hours, using three nests with resolutions of 27, 9, and 3 km. In the 3 km domain, only the cloud microphysical parameterization scheme was used [for simulation verification and other details, see Li et al. (2014)], and the cloud microphysical data (including cloud microphysical conversion terms) were output and analyzed in this study.

2.2. *Cloud microphysical scheme*

The cloud microphysical scheme used was the Milbrandt 2-mom scheme (Milbrandt and Yau, 2005a, b), which includes water vapor and six cloud species: water vapor (Q_v); cloud water (Q_c); rain water (Q_r); cloud ice (Q_i); snow (Q_s); graupel (Q_g); and hail (Q_h). Figure 1 shows the microphysical flowchart for the Milbrandt 2-mom scheme [for detailed microphysical conversion processes, see Milbrandt and Yau (2005b)]. The tendencies for the mixing ratios are

$$\begin{aligned}
S_{Q_v} &= -\mathrm{QVD_{vc}} - \mathrm{QVD_{vr}} - \mathrm{QNU_{vi}} - \mathrm{QVD_{vi}} - \\
&\quad \mathrm{QVD_{vs}} - \mathrm{QVD_{vg}} - \mathrm{QVD_{vh}} , \qquad (1)\\
S_{Q_c} &= \mathrm{QVD_{vc}} - \mathrm{QCN_{cr}} - \mathrm{QCL_{cr}} - \mathrm{QFZ_{ci}} - \\
&\quad \mathrm{QCL_{ci}} - \mathrm{QCL_{cs}} - \mathrm{QCL_{cg}} - \mathrm{QCL_{ch}} , \qquad (2)\\
S_{Q_r} &= \mathrm{QCN_{cr}} + \mathrm{QCL_{cr}} + \mathrm{QVD_{vr}} + \mathrm{QML_{ir}} + \\
&\quad \mathrm{QML_{sr}} + \mathrm{QML_{gr}} + \mathrm{QML_{hr}} - \mathrm{QCL_{ri}} - \\
&\quad \mathrm{QCL_{rs}} - \mathrm{QCL_{rg}} - \mathrm{QCL_{rh}} - \mathrm{QFZ_{rh}} , \qquad (3)\\
S_{Q_i} &= \mathrm{QNU_{vi}} + \mathrm{QFZ_{ci}} + \mathrm{QVD_{vi}} + \mathrm{QIM_{si}} + \mathrm{QIM_{gi}} + \\
&\quad \mathrm{QCL_{ci}} - \mathrm{QCL_{ir}} - \mathrm{QCL_{is}} - \mathrm{QCL_{ig}} - \mathrm{QCL_{ih}} - \\
&\quad \mathrm{QCN_{is}} - \mathrm{QCN_{ig}} - \mathrm{QML_{ir}} , \qquad (4)\\
S_{Q_s} &= \delta_{\mathrm{srs}}(\mathrm{QCL_{rs}} + \mathrm{QCL_{sr}}) + \mathrm{QCN_{is}} + \mathrm{QVD_{vs}} + \\
&\quad \mathrm{QCL_{cs}} + \mathrm{QCL_{is}} - \mathrm{QCN_{sg}} - \mathrm{QCL_{sr}} - \mathrm{QCL_{sh}} - \\
&\quad \mathrm{QIM_{si}} - \mathrm{QML_{sr}} , \qquad (5)\\
S_{Q_g} &= \delta_{\mathrm{irg}}(\mathrm{QCL_{ir}} + \mathrm{QCL_{ri}}) + \delta_{\mathrm{srg}}(\mathrm{QCL_{sr}} + \mathrm{QCL_{rs}}) + \\
&\quad \delta_{\mathrm{grg}}(\mathrm{QCL_{gr}} + \mathrm{QCL_{rg}}) + \mathrm{QCN_{ig}} + \mathrm{QCN_{sg}} + \\
&\quad \mathrm{QCL_{cg}} + \mathrm{QCL_{ig}} - \mathrm{QCL_{gr}} + \mathrm{QVD_{vg}} - \\
&\quad \mathrm{QCN_{gh}} - \mathrm{QML_{gr}} - \mathrm{QIM_{gi}} , \qquad (6)\\
S_{Q_h} &= \delta_{\mathrm{irh}}(\mathrm{QCL_{ir}} + \mathrm{QCL_{ri}}) + \delta_{\mathrm{srh}}(\mathrm{QCL_{sr}} + \mathrm{QCL_{rs}}) + \\
&\quad \delta_{\mathrm{grh}}(\mathrm{QCL_{gr}} + \mathrm{QCL_{rg}}) + \mathrm{QFZ_{rh}} + \mathrm{QCN_{gh}} + \\
&\quad \mathrm{QCL_{ch}} + \mathrm{QCL_{rh}} + \mathrm{QCL_{ih}} + \mathrm{QCL_{sh}} + \\
&\quad \mathrm{QVD_{vh}} - \mathrm{QML_{hr}} , \qquad (7)
\end{aligned}$$

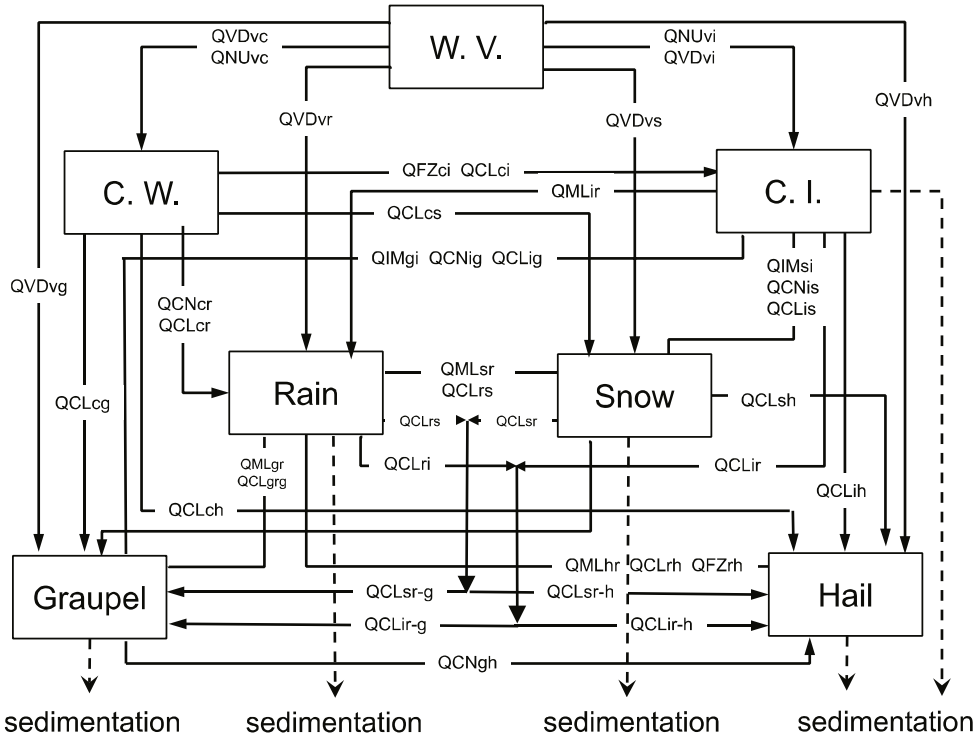

Fig. 1. Microphysical flowchart for the Milbrandt 2-mom scheme. The rectangles represent the various water species (water vapor, cloud water, rain water, cloud ice, snow, graupel, hail), and the arrows are the processes that link the species.

where $S_{Q_v}, S_{Q_c}, S_{Q_r}, S_{Q_i}, S_{Q_s}, S_{Q_g}$ and S_{Q_h} are microphysical source/sink terms of water vapor and cloud species, respectively. The notation for the terms involving two interacting categories is denoted by QAB_{yx} (also see Milbrandt and Yau, 2005b), where Q is the prognostic variable mass mixing ratio, AB represents microphysical processes (QCL for collection, QCN for conversion, QFZ for freezing, QIM for ice multiplication, QML for melting, QNU for nucleation, QSH for shedding, QVD for diffusional growth), and the subscript "yx" indicates that mass is being transferred from category y to x [$x, y \in (v, c, r, i, s, g, h)$ denote various water species]. δ_{xry} is a determination coefficient meaning that category x (s, i, g) and raindrops collide to form category y (s, g, h). For example, if raindrops and snow collide to form graupel, then $\delta_{\mathrm{srg}} = 1, \delta_{\mathrm{srs}} = 0$ and $\delta_{\mathrm{srh}} = 0$ (for details, see Milbrandt and Yau, 2005b).

3. Results

3.1. *Precipitation and cloud hydrometeors distribution*

Figure 2 shows the distributions of 6-hourly accumulated rainfall and 6-hourly averaged and vertically integrated[a] mixing ratios of hydrometeors in the weak (0000–0600 UTC 18 August 2010) and strong (1800 UTC 18 August to 0000 UTC 19 August 2010) precipitation periods. The mixing ratio of hail was negligibly small in this rainfall event and is not analyzed in the following discussions. In the strong precipitation period, the area and intensity of precipitation and cloud hydrometeors increased compared with those in the weak precipitation period (Fig. 2). In the weak precipitation period, 6-hourly accumulated rainfall did not exceed 40 mm, compared to the maximum 6-hourly accumulated rainfall of over 100 mm in the strong precipitation period (Figs. 2a and b). As for the 6-hourly averaged and vertically integrated mixing ratios of hydrometeors, the maximum of the mixing ratios increased from less than 0.09×10^{-3} kg kg^{-1} to more than 0.27×10^{-3} kg kg^{-1} for cloud water (Figs. 2c and d), from less than 0.06×10^{-3} kg kg^{-1} to more than 0.3×10^{-3} kg kg^{-1} for rain water (Figs. 2e and f), from less than 0.06×10^{-3} kg kg^{-1} to more than 0.14×10^{-3} kg kg^{-1} for cloud ice (Figs. 2g and h), from less than 0.2×10^{-3} kg kg^{-1} to more than 0.7×10^{-3} kg kg^{-1} for snow (Figs. 2i and 2j), and from less than 0.04×10^{-3} kg kg^{-1} to more than 0.6×10^{-3} kg kg^{-1} for graupel (Figs. 2k and l). In the strong precipitation period, the centers of the rain water mixing ratio coincided well with rainfall centers as well as cloud water, snow and graupel, indicating that the evolutions of both liquid and solid hydrometeors may have important contributions to precipitation development. Compared with the weak precipitation period, in the strong precipitation period, not only liquid hydrometeors (cloud water and rain water) increased significantly (the

[a]Integral calculation method: $Q_{x,\mathrm{vint}} = \int_{p_s}^{p_t} Q_x dp/(p_t - p_s)$ where, $Q_{x,\mathrm{vint}}$ represents vertically integrated mixing ratio of category x (Q_x), P_t and P_s are pressure at the top and the surface of the atmosphere.

maximum growth of cloud water content was more than three times greater, and the maximum growth of rain water content was more than five times greater), but also solid hydrometeors (cloud ice, snow and graupel) grew significantly (the maximum growth of cloud ice content was more than two times greater, the maximum growth of snow was more than three times greater, and the maximum growth of graupel was more than fifteen times greater), and their centers were consistent with strong rainfall centers, showing that cold cloud processes developed remarkably and ice-phase processes contributed much more to the rainfall in the strong precipitation period.

3.2. *Cloud microphysical characteristics*

To further study the differences in cloud microphysical characteristics between the weak and strong precipitation periods, we focused our analysis on the region of (28°–33°N, 100°–106°E) in the 3 km domain. Grids whose 6-hourly accumulated rainfall was greater than 35 mm (256 grids in total) in the weak precipitation period (0000–0600 UTC 18

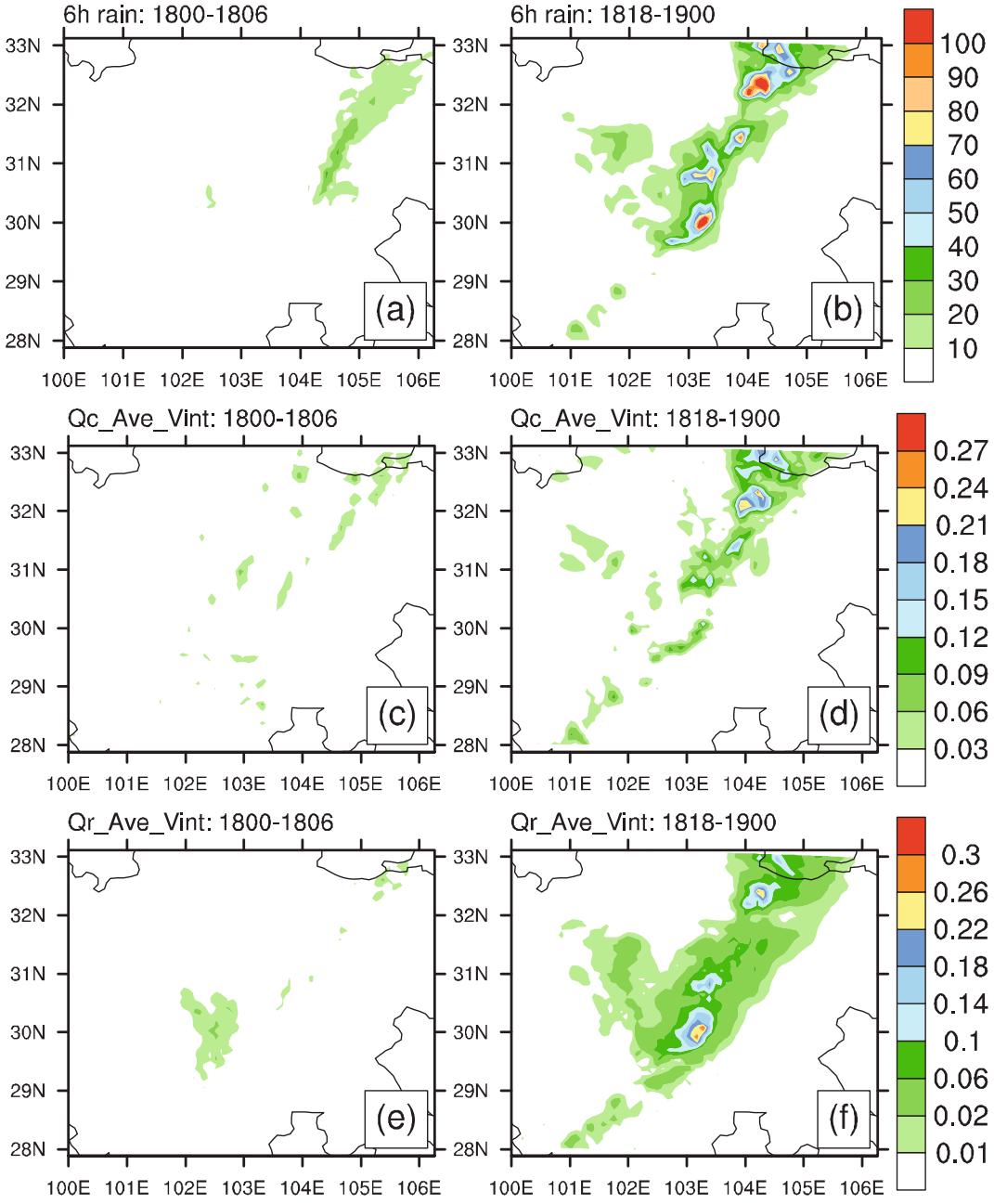

Fig. 2. Distribution of (a, b) 6-hourly accumulated rainfall (units: mm) and 6-hourly averaged and vertically integrated hydrometeors mixing ratios [(c, d) cloud water; (e, f) rain water; (g, h) cloud ice; (i, j) snow; (k, l) graupel (units: 10^{-3} kg kg^{-1})] in the weak precipitation period (0000–0600 UTC 18 Aug 2010, left column) and the strong precipitation period (1800 UTC 18 Aug–0000 UTC 19 Aug 2010, right column).

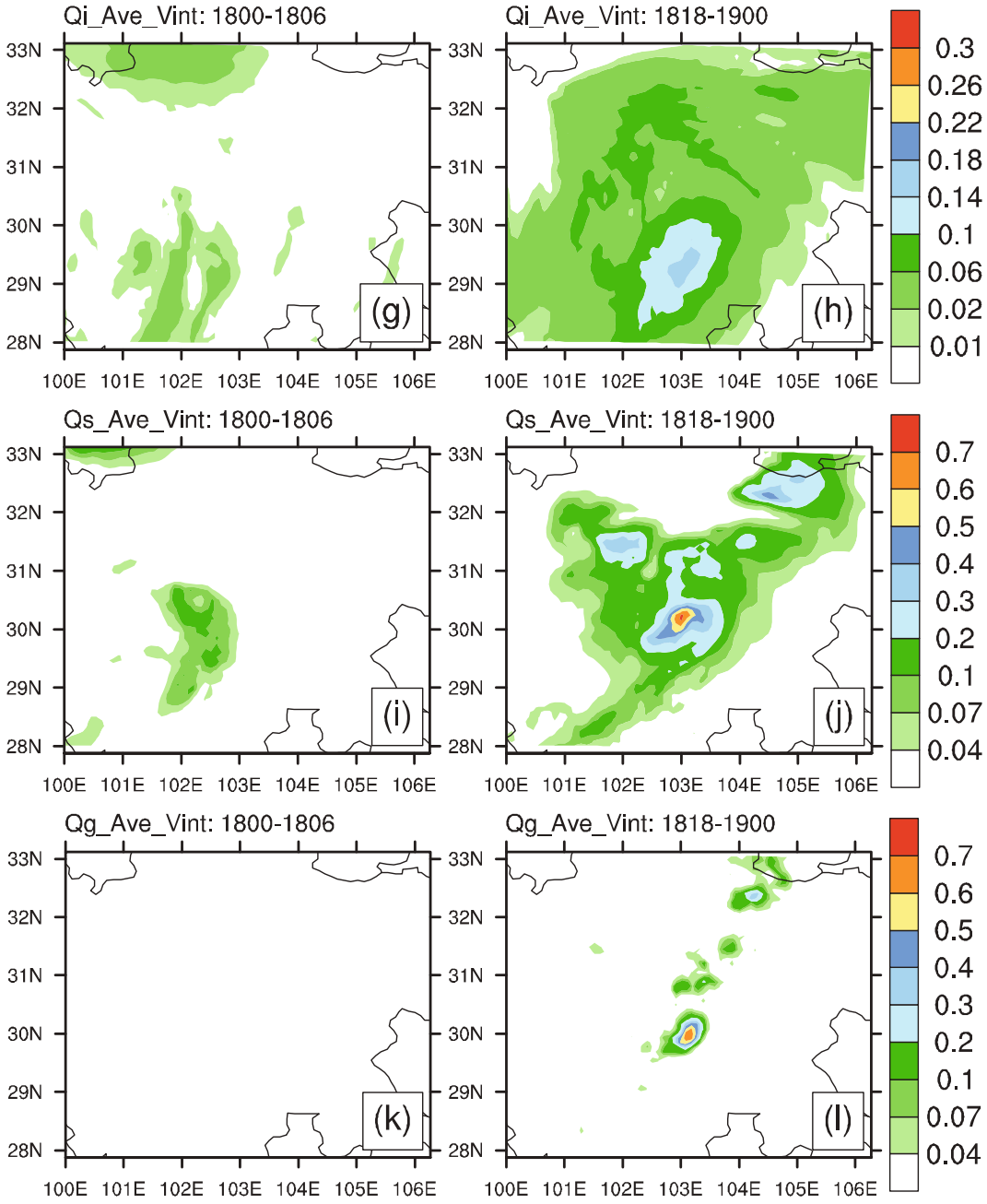

Fig. 2. (Continued.)

August 2010) and grids whose 6-hourly accumulated rainfall was greater than 80 mm (228 grids in total) in the strong precipitation period (1800 UTC 18 August to 0000 UTC 19 August 2010) were chosen for analysis.

Figure 3 shows composites of vertical profiles of hydrometeor mixing ratios (Figs. 3a and b), number concentrations (Figs. 3c and d), mean-mass diameters (Figs. 3e and f), and terminal velocities and air vertical velocities (Figs. 3g and h) in the weak and strong precipitation periods. In the Milbrandt 2-mom scheme, the mean-mass diameter D_{mx} for each hydrometeor category x was computed by

$$D_{mx} = \left(\frac{\rho Q_x}{c_x N_x}\right)^{1/d_x}, \tag{8}$$

where ρ is the air density, c_x and d_x are parameters for the mass–diameter relations [see Milbrandt and Yau (2005a) for specific values], Q_x is the mixing ratio, and N_x is the total number concentration. Tables 1 and 2 show the vertical accumulations of the above profiles of mixing ratios and number concentrations, respectively. In the weak precipitation period, graupel was the most abundant (3.9036), the mixing ratios of cloud water (2.5644) and rain water (2.3247) were similar, and cloud ice (0.6282) and snow (0.7426) were the least prevalent (Fig. 3a, Table 1). In the strong precipitation period, the abundance of the main hydrometeors increased significantly (Fig. 3b). The ratios of the mixing ratios of cloud water, rain water, cloud ice, snow and graupel between the weak and strong precipitation periods were 1.6170,

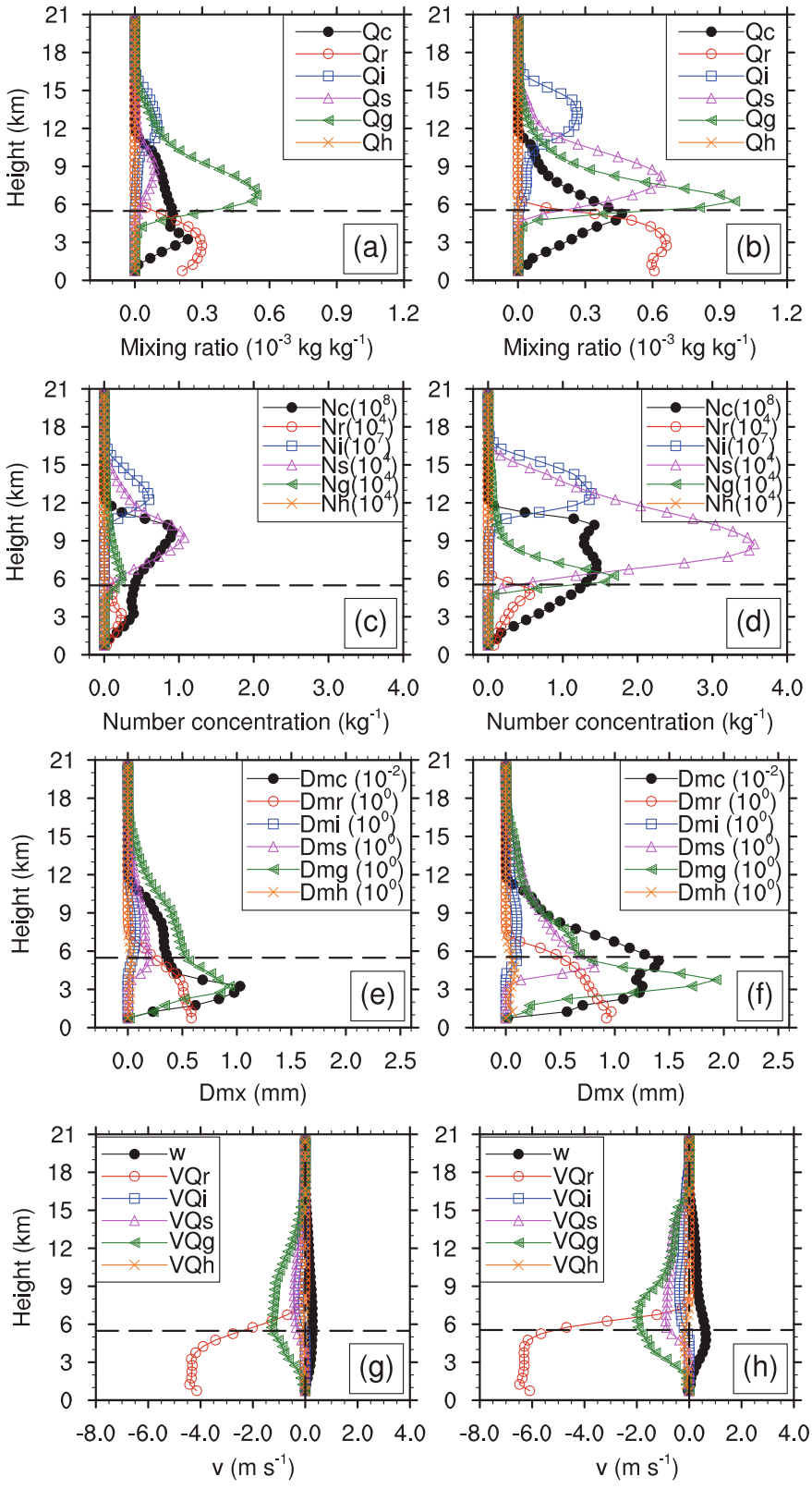

Fig. 3. Vertical profiles of (a, b) hydrometeor mixing ratios (units: 10^{-3} kg kg^{-1}), (c, d) number concentrations (units: kg^{-1}, see annotation for orders of magnitude), (e, f) mean-mass diameters (units: mm, see annotation for orders of magnitude), and (g, h) terminal velocities and air vertical velocity (units: m s^{-1}) in the weak precipitation period (0000–0600 UTC 18 Aug 2010, left column) and the strong precipitation period (1800 UTC 18 Aug–0000 UTC 19 Aug 2010, right column). Dashed lines represents the 0°C isotherm.

2.5864, 5.1195, 9.0687 and 1.7009, respectively (Table 1). A larger rain water mixing ratio (6.0126) corresponded with the strong precipitation. Higher snow (6.7344) and graupel (6.6396) mixing ratios may have made an important contribution to the development of the cloud system and strong precipitation; compared with the weak precipitation period, the higher cloud water mixing ratio (4.1467) in the strong precipitation period may also have played an important role in the strong surface precipitation (Fig. 3b, Table 1). Furthermore, as shown in Figs. 3a and b, and the vertically stratified accumulation results in Tables 1 and 2, the cloud water above and below the zero layer possessed similar magnitudes, and abundant super-cooled cloud water may have made an important contribution to the heavy rainfall. Rain water (cloud ice, snow and graupel) was mainly distributes below (above) the zero layer, and the coalescence of cloud water and rain water below the zero layer should also plays an important role in strong rainfall. There was also some graupel distributed below the zero degree layer, whose melting may have made an important contribution to the growth of rain water and the enhancement of surface rainfall.

As shown in Figs. 3e and f, in the strong precipitation period, particle sizes of all hydrometeors increased compared with those in the weak precipitation period, and mean-mass diameters of graupel increased the most significantly (maximum increased from about 0.9 mm to more than 1.9 mm), while the increase in the mean-mass diameters of cloud ice was not significant. In Eq. (8), the mean-mass diameter D_{mx} is not only correlated with the number concentration N_x, but also with the mixing ratio Q_x. Although the number concentrations of all hydrometeors increased (Figs. 3c and d, Table 2), their mixing ratios increased as well (Figs. 3a and b, Table 1). Therefore, the ratio of the mixing ratio Q_x to the number concentration N_x for each hydrometer increased (but with distinctly different magnitudes), indicating that the mean-mass diameter increased, thereby increasing the mean particle size (Figs. 3e and f). The increasing of graupel particle sizes may be partially related to the accretion of cloud water by graupel to form graupel, which causes the graupel mixing ratio to increase while the graupel number concentration remains roughly the same. Similarly, the increasing of rain water particle sizes may be partially related to the accretion of cloud water by rain water to form rain water. Besides, the increasing of particle sizes of all hydrometeors is favorable for the occurrence of collision between particles, especially cloud water with rain water and graupel.

Meanwhile, Figs. 3c and d show that the height of the number concentration maximum of cloud water and rain water in the strong precipitation period was higher than in the weak precipitation period. This may have been related to stronger vertical upward motion in the strong precipitation period (Figs. 3g and h). By analyzing the vertical profiles of vertical velocity of air and various hydrometeors' terminal velocities in the two periods (Figs. 3g and h), we can see that

Table 1. Vertical cumulative mixing ratios of cloud hydrometeors ($Q_v, Q_c, Q_r, Q_i, Q_s, Q_g, Q_h$, units: 10^{-3} kg kg^{-1}) throughout the whole layer, above and below the zero layer, in the weak precipitation period (0000–0600 UTC 18 Aug 2010) and the strong precipitation period (1800 UTC 18 Aug–0000 UTC 19 Aug 2010). The ratio is (1818–1900)/(1800–1806).

	Period	Q_c	Q_r	Q_i	Q_s	Q_g	Q_h
Whole layer	1800–1806	2.5644	2.3247	0.6282	0.7426	3.9036	0.0003
	1818–1900	4.1467	6.0126	3.2161	6.7344	6.6396	0.0002
	Ratio	1.6170	2.5864	5.1195	9.0687	1.7009	0.6667
Above zero layer	1800–1806	1.2212	0.0448	0.6280	0.7253	3.5417	0.0001
	1818–1900	1.8684	0.1327	3.2149	6.6105	6.1577	0.0001
	Ratio	1.5300	2.9621	5.1193	9.1142	1.7386	1.0000
Below zero layer	1800–1806	1.3432	2.2799	0.0002	0.0173	0.3619	0.0002
	1818–1900	2.2783	5.8799	0.0012	0.1239	0.4819	0.0001
	Ratio	1.6962	2.5790	6.0000	7.1618	1.3316	0.5000

Table 2. Vertical cumulative number concentrations of cloud hydrometeors ($N_c, N_r, N_i, N_s, N_g, N_h$, units: kg^{-1}) throughout the whole layer, above and below the zero layer, in the weak precipitation period (0000–0600 UTC 18 Aug 2010) and the strong precipitation period (1800 UTC 18 Aug–0000 UTC 19 Aug 2010). The ratio is (1818–1900)/(1800–1806).

	Period	N_c (10^8)	N_r (10^4)	N_i (10^7)	N_s (10^4)	N_g (10^4)	N_h (10^4)
Whole layer	1800–1806	9.7661	1.5266	3.1795	9.5038	1.5795	0.0000
	1818–1900	20.0584	3.0935	11.4094	43.8504	8.9753	0.0000
	Ratio	2.0539	2.0264	3.5884	4.6140	5.6824	
Above zero layer	1800–1806	6.9468	0.0670	3.1795	9.4014	1.4066	0.0000
	1818–1900	13.7587	0.2653	11.4091	43.6404	8.1962	0.0000
	Ratio	1.9806	3.9597	3.5883	4.6419	5.8270	
Below zero layer	1800–1806	2.8193	1.4596	0.0000	0.1024	0.1729	0.0000
	1818–1900	6.2997	2.8282	0.0003	0.2100	0.7791	0.0000
	Ratio	2.2345	1.9377		2.0508	4.5061	

the rain water's terminal velocity was the strongest among all hydrometeors in both the strong (strongest value was close to -6.5 m s^{-1}) and weak (strongest value was close to -4.5 m s^{-1}) precipitation periods. Graupel's terminal velocity was second strongest, but its strongest value was only about -2 m s^{-1} (in the strong precipitation period), far below that of rain water. In the strong precipitation period, the differences among the various hydrometeors' terminal velocities became larger compared to in the weak precipitation period, which would have been more beneficial to relative motion, coalescence and transformation between particles. It is worth noting that the absolute values of the rain water's and graupel's terminal velocities were significantly greater than that of air vertical velocity, and the stronger the precipitation was, the larger the differences between them were (Figs. 3g and h). This was the result of the development of the cloud microphysical processes during the rainstorm, which may have presaged the gradual demise of the storm cloud system and the gradual end of the rainstorm process.

3.3. *Cloud microphysical conversion processes*

The microphysical sources/sinks and conversion processes of hydrometeors in the weak and strong precipitation periods are shown in Fig. 4. The hydrometeors' main microphysical sources/sinks were similar in both periods, but the sources/sinks in the strong precipitation period were significantly stronger than those in the weak precipitation period, ultimately resulting in differences in the intensity of precipitation. Furthermore, the orders of magnitude of the sources/sinks (cloud microphysical conversion rates) of water vapor, cloud water, rain water and graupel were much larger than those of cloud ice and snow, indicating that water vapor, cloud water, rain water, graupel and their conversion processes played a major role during the development of the rainstorm. Condensation of water vapor to form cloud water ($\mathrm{QVD_{vc}}$) was the main source term of cloud water, while accretion of cloud water by rain water ($\mathrm{QCL_{cr}}$) and the accretion of cloud water by graupel ($\mathrm{QCL_{cg}}$) were the main sink terms of cloud water (Figs. 4c and d). In the budget of graupel, the collection of cloud water by graupel ($\mathrm{QCL_{cg}}$) was a main source term of graupel, while the melting of graupel to form rain water ($\mathrm{QML_{gr}}$) was a major consumption term of graupel (Figs. 4k and l). The graupel production from the process of graupel–rain collision ($\mathrm{QCL_{grg}}$) required the expenditure of graupel ($\mathrm{QCL_{gr}}$) and rain water ($\mathrm{QCL_{rg}}$). Therefore, the net growth of graupel by graupel–rain collision and coalescence was ($\mathrm{QCL_{grg}} - \mathrm{QCL_{gr}}$). Meanwhile, since absolute values of $\mathrm{QCL_{grg}}$ and $\mathrm{QCL_{gr}}$ were similar (Figs. 4k and l), values of ($\mathrm{QCL_{grg}} - \mathrm{QCL_{gr}}$) were small, meaning that the collection of rain water by graupel to form graupel was not a main source/sink term of graupel (Figs. 4k and l). As for rain water, the accretion of cloud water by rain water ($\mathrm{QCL_{cr}}$) and the melting of graupel to form rain water ($\mathrm{QML_{gr}}$) were the main source terms (Figs. 4e and f), which caused the rapid growth of rain water (Fig. 4f) and eventually enhanced surface precipitation in the strong precipitation period (Fig. 2b).

The above analysis of hydrometeors' microphysical sources/sinks is summarized in Fig. 5. The solid thick arrows (Fig. 5) represent the most important microphysical conversion processes in this rainstorm. The main cloud microphysical conversion processes related to precipitation in the two periods were the same, shown as solid thick arrows in Fig. 5, and proportions of these processes to total water vapor loss (WVL[b], Colle and Zeng, 2004) in each period were roughly equal (see the values on the right-hand sides of the conversion process notations in Fig. 5). However, due to different total water vapor loss rates in the strong (WVL = 15.73) and weak (WVL = 7.38) precipitation periods, the microphysical conversion rates between these two periods were significantly different (see values in parentheses in Fig. 5), resulting in significant differences in precipitation intensity between these two periods. In the strong precipitation period (Fig. 5b), there were two main pathways to generate rain water: $\mathrm{QVD_{vc}} \rightarrow \mathrm{QCL_{cr}}$ and $\mathrm{QVD_{vc}} \rightarrow \mathrm{QCL_{cg}} \rightarrow \mathrm{QML_{gr}}$, which can be described as follows: Abundant water vapor condensed into cloud water ($\mathrm{QVD_{vc}}$) and, on the one hand, accretion of cloud water by rain water ($\mathrm{QCL_{cr}}$) formed rain water, while on the other hand, accretion of cloud water by graupel ($\mathrm{QCL_{cg}}$) formed graupel, and then the melting of graupel formed rain water ($\mathrm{QML_{gr}}$). As discussed above, the net growth of graupel by graupel–rain water collision and coalescence ($\mathrm{QCL_{grg}} - \mathrm{QCL_{gr}}$) was not a major source of graupel and was also not a major sink of rain water (Fig. 5). Therefore, the net result of ($\mathrm{QCL_{grg}} - \mathrm{QCL_{gr}}$) contributed little to raindrop growth and enhancement of surface precipitation. In Fig. 5, we can see another distinct difference between the two periods: In the strong precipitation period, depositional growth of snow ($\mathrm{QVD_{vs}}$), melting of snow to form rain water ($\mathrm{QML_{sr}}$), and autoconversion (aggregation) of snow to form graupel ($\mathrm{QCN_{sg}}$) strengthened, which played a role in the growth of rain water (Fig. 5b). Due to the accumulation of abundant moisture in the strong precipitation period, water vapor deposition to form ice-phase particles, such as snow ($\mathrm{QVD_{vs}}$), was more likely to occur in the upper levels. Meanwhile, in the strong precipitation period, mixing ratios of cloud water and snow were significantly larger than those in the weak precipitation period (Figs. 3a and b), so the accretion of cloud water by snow ($\mathrm{QCL_{cs}}$) strengthened (Fig. 5). The increasing of snow also had an active effect on the autoconversion of snow to form graupel. Besides, from Fig. 3b, we can see that the vertical profile of the snow mixing ratio extended below the zero layer, thereby enhancing the process of snow melting into rain water. However, the orders of magnitudes of these conversion processes associated with snow were significantly smaller than those of the main

[b] WVL, Water Vapor Loss is defined as

$$\mathrm{WVL} = \max(\mathrm{QVD_{vc}}, 0) + \max(\mathrm{QVD_{vr}}, 0) + \max(\mathrm{QNU_{vi}}, 0) + \max(\mathrm{QVD_{vi}}, 0) + \max(\mathrm{QVD_{vs}}, 0) + \max\left(\mathrm{QVD_{vg}}, 0\right) + \max(\mathrm{QVD_{vh}}, 0)$$

microphysical conversion processes mentioned above.

4. Summary

In this study, by using high-resolution numerical simulation data of an orographic torrential rainfall process in Sichuan simulated by the WRF model, differences of cloud microphysical characteristics and conversion processes between weak and strong precipitation periods were analyzed to investigate the dominant cloud microphysical processes responsible for the development of the torrential rainfall. The major results can be summarized as follows:

(1) In the strong precipitation period, the area and intensity of precipitation and cloud hydrometeors increased compared with those in the weak precipitation period, and the centers of rain water, cloud water and graupel were collo-

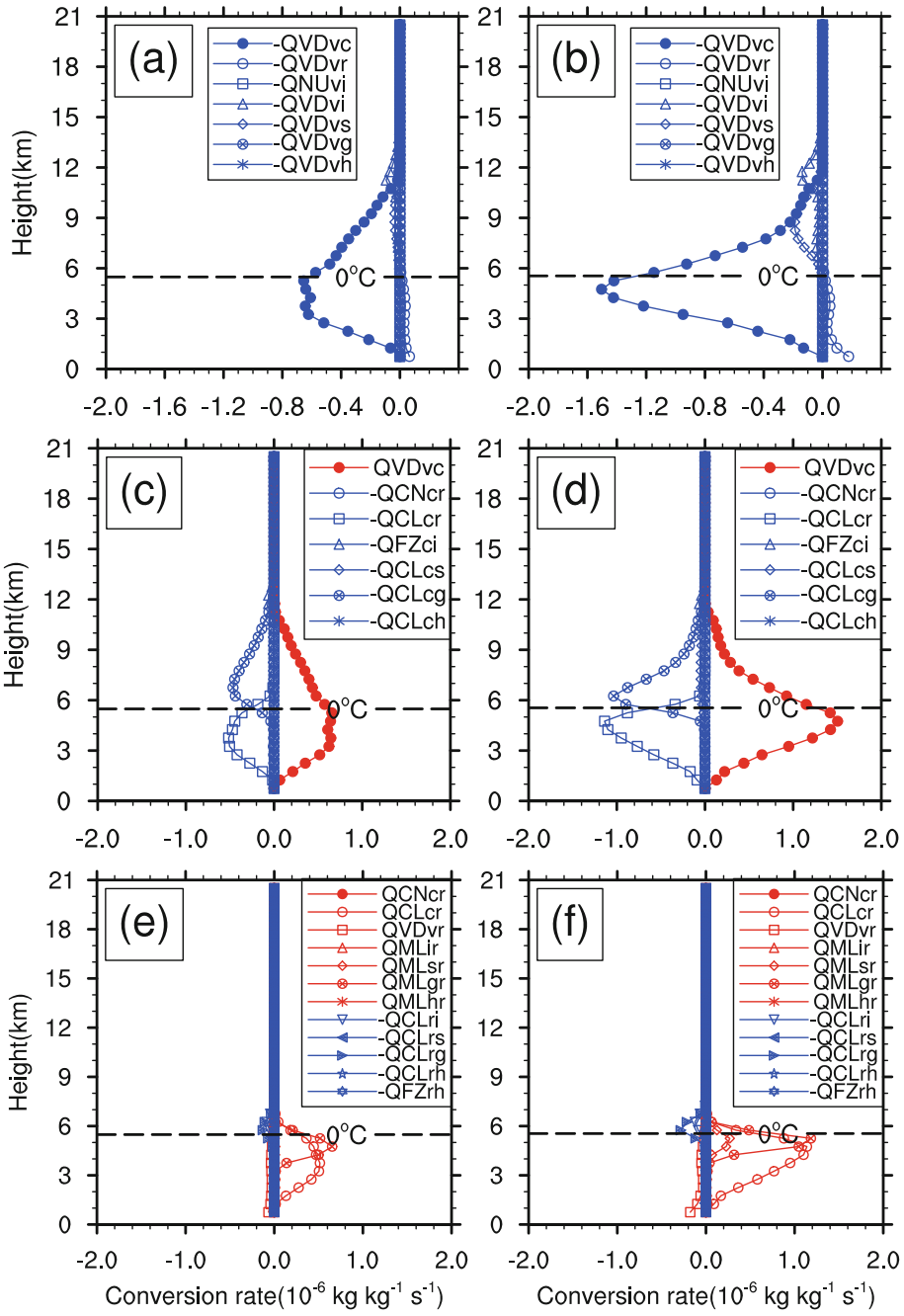

Fig. 4. Vertical profiles of budgets of various water species [(a, b) water vapor; (c, d) cloud water; (e, f) rain water; (g, h) cloud ice; (i, j) snow; (k, l) graupel (units: 10^{-6} kg kg^{-1} s^{-1})] in the weak precipitation period (0000–0600 UTC 18 Aug 2010, left column) and the strong precipitation period (1800 UTC 18 Aug–0000 UTC 19 Aug 2010, right column). Dashed lines represents the 0°C isotherm.

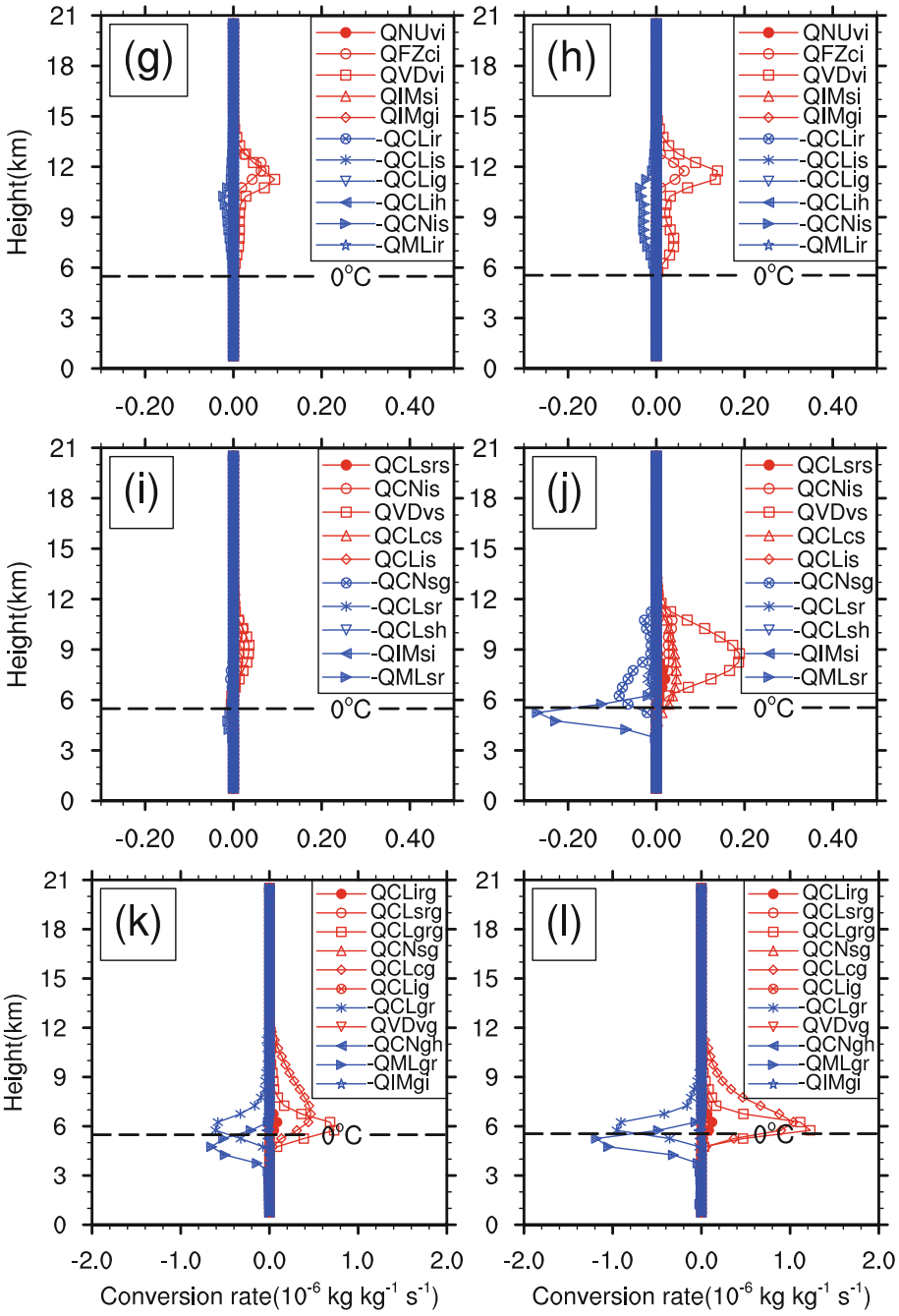

Fig. 4. (Continued.)

cated with strong rainfall centers, showing that both liquid and solid hydrometeors may play an important role in surface precipitation.

(2) Composite analysis of cloud hydrometeors revealed that, in the strong precipitation period, the cloud hydrometeors increased significantly. Abundant super-cooled cloud water may have made an important contribution to heavy rainfall. The coalescence of cloud water and rain water below the zero layer and the melting of graupel may also have played important roles in the growth of rain water and the enhancement of surface rainfall. In the strong precipitation period, particle sizes of all hydrometeors increased, especially graupel's. The increasing of particle sizes of all hydrometeors was favorable to the occurrence of collision between particles, especially cloud water with rain water and graupel.

(3) The terminal velocity of raindrops was the strongest among all hydrometeors in both the weak and strong precipitation periods, followed by that of graupel. Differences of terminal velocities among the various hydrometeors in the strong precipitation period were larger than those in the weak precipitation period, which was favorable for the relative motion, collection interaction and exchange between particles. Absolute values of terminal velocities of raindrops and graupel were significantly greater than those of air updrafts. The

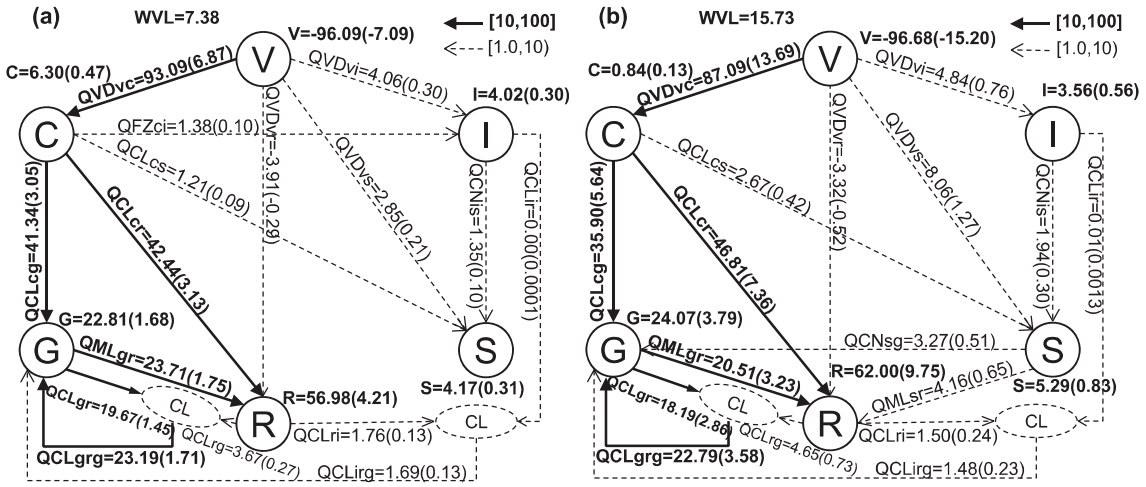

Fig. 5. Microphysical flowchart for the (a) weak precipitation period (0000–0600 UTC 18 Aug 2010) and (b) strong precipitation period (1800 UTC 18 Aug–0000 UTC 19 Aug 2010). On the right-hand side of each microphysical conversion process notation, the values outside the brackets are the ratio of the vertically cumulative conversion rate to total water vapor loss rate (WVL) (units: %; thick solid arrows show ratios greater than 10%, dotted arrows show ratios between 1% and 10%, and values less than 1% are omitted), while the values inside the brackets are the microphysical conversion rates (units: 10^{-6} kg kg^{-1} s^{-1}). The sum of all the microphysical process tendencies for each species is given by V (water vapor), C (cloud water), R (rain water), I (cloud ice), S (snow) and G (graupel) (due to the small order of magnitude, hail is omitted).

stronger the precipitation was, the greater the differences between them were, which may imply a decay of the rainfall.

(4) In both periods, the budgets of cloud microphysics were similar, but the orders of magnitudes of the cloud microphysical conversion terms in the strong precipitation period were significantly larger than those in the weak precipitation period, resulting in a difference in the intensity of surface rainfall. Besides, the orders of magnitude of the conversion rates of water vapor, cloud water, rain water and graupel were much larger than those of cloud ice and snow, showing that water vapor, cloud water, rain water and graupel and their conversion processes may have played a major role in the development of the torrential rainfall event.

(5) In the rainstorm process, there were two main pathways for the generation of raindrops: $\mathrm{QVD_{vc}} \rightarrow \mathrm{QCL_{cr}}$ and $\mathrm{QVD_{vc}} \rightarrow \mathrm{QCL_{cg}} \rightarrow \mathrm{QML_{gr}}$. In detail, abundant water vapor condensed into cloud water ($\mathrm{QVD_{vc}}$) and, on the one hand, the accretion of cloud water by rain water ($\mathrm{QCL_{cr}}$) formed rain water, while on the other hand, the accretion of cloud water by graupel ($\mathrm{QCL_{cg}}$) formed graupel, and then the melting of graupel formed rain water ($\mathrm{QML_{gr}}$). Furthermore, the net growth of graupel by graupel–rain water collision and coalescence ($\mathrm{QCL_{grg}} - \mathrm{QCL_{gr}}$) contributed little to raindrop growth and enhancement of surface precipitation.

Our own previous analyses and studies have shown that the type of orographic torrential rainfall discussed in this study is very common in summer in the Sichuan region. Thus, although only one case has been analyzed in this paper, the conclusions may have a certain degree of universality, which is of great significance as we strive for an in-depth and comprehensive understanding of the mechanisms underpinning orographic torrential rainfall in the Sichuan region. In future work, we will analyze more cases to make the conclusions more robust and statistically significant.

Acknowledgements. This work was supported by the Key Research Program of the Chinese Academy of Sciences (Grant No. KZZD-EW-05-01) and the National Basic Research Program of China (973 Program) (Grant No. 2014CB441402).

REFERENCES

Chen, C. P., H. Z. Feng, and J. Chen, 2010: Application of Sichuan heavy rainfall ensemble prediction probability products based on Bayesian method. *Meteorological Monthly*, **36**(5), 32–39. (in Chinese)

Chen, Y. R., and Y. Q. Li, 2013: Characteristics of mesoscale convective system and its effects on short-time severe rainfall in Sichuan Basin during 21–22 July 2012. *Meteorological Monthly*, **39**(7), 848–860. (in Chinese)

Colle, B. A., and Y. G. Zeng, 2004: Bulk microphysical sensitivities within the MM5 for orographic precipitation. Part II: Impact of barrier width and freezing level. *Mon. Wea. Rev.*, **132**, 2802–2815.

Crochet, P., T. Jóhannesson, T. Jónsson, O. Sigurðsson, H. Björnsson, F. Pálsson, and I. Barstad, 2007: Estimating the spatial distribution of precipitation in Iceland using a linear model of orographic precipitation. *J. Hydrometeor.*, **8**, 1285–1306.

Ge, J. J., W. Zhong, N. Du, and H. C. Lu, 2008: Numerical simulation and analysis of Sichuan rainstorm under terrain influence. *Scientia Meteorologica Sinica*, **28**(2), 176–183. (in Chinese)

He, Y., and G. P. Li, 2013: Numerical experiments on influence of Tibetan Plateau on persistent heavy rain in South China. *Chinese J. Atmos. Sci.*, **37**(4), 933–944. (in Chinese)

Li, A. T., and H. R. He, 2011: Impact of different cloud microphys-

ical parameterization schemes on the numeric simulation results of "8.8" rainstorm process in Zhouqu. *Meteorology and Disaster Reduction Research*, **34**(3), 9–16. (in Chinese)

Li, Q., X. P. Cui, and J. Cao, 2014: The observational analysis and numerical simulation of a heavy rain event in Sichuan Province. *Chinese J. Atmos. Sci.*, doi: 10.3878/j.issn.1006-9895.1401.13255. (in Chinese)

Liao, J. B., X. M. Wang, B. C. Xia, T. J. Wang, and Z. M. Wang, 2012: The effects of different physics and cumulus parameterization schemes in WRF on heavy rainfall simulation in PRD. *J. Trop. Meteor.*, **28**(4), 461–470. (in Chinese)

Lu, P., R. C. Yu, and T. J. Zhou, 2009: Numerical simulation on the sensitivity of heavy rainfall over the western Sichuan Basin to initial water vapor condition. *Chinese J. Atmos. Sci.*, **33**(2), 241–250. (in Chinese)

Ma, Y. Z., C. G. Lu, and S. T. Gao, 2012: The effects of different microphysical schemes in WRF on a heavy rainfall in North China during 18–19 August 2010. *Chinese J. Atmos. Sci.*, **36**(4), 835–850. (in Chinese)

Maussion, F., D. Scherer, R. Finkelnburg, J. Richters, W. Yang, and T. D. Yao, 2010: WRF simulation of a precipitation event over the Tibetan Plateau, China—An assessment using remote sensing and ground observations. *Hydrology and Earth System Sciences Discussions*, **15**, 1795–1817.

Milbrandt, J. A., and M. K. Yau, 2005a: A multimoment bulk microphysics parameterization. Part I: Analysis of the role of the spectral shape parameter. *J. Atmos. Sci.*, **62**, 3051–3064.

Milbrandt, J. A., and M. K. Yau, 2005b: A multimoment bulk microphysics parameterization. Part II: A proposed three-moment closure and scheme description. *J. Atmos. Sci.*, **62**, 3065–3081.

Sawyer, J. S., 1956: The physical and dynamical problems of orographic rain. *Weather*, **11**(12), 375–381.

Smith, B. L., S. E. Yuter, P. J. Neiman, and D. E. Kingsmill, 2010: Water vapor fluxes and orographic precipitation over Northern California associated with a landfalling atmospheric river. *Mon. Wea. Rev.*, **138**, 74–100.

Smith, R. B., and I. Barstad, 2004: A linear theory of orographic precipitation. *J. Atmos. Sci.*, **61**, 1377–1391.

Smith, R. B., and J. P. Evans, 2007: Orographic precipitation and water vapor fractionation over the Southern Andes. *J. Hydrometeor.*, **8**, 3–19.

Wang, C. X., S. T. Gao, L. Liang, and Y. Z. Ma, 2013: Diagnostic analysis of dynamical parameters for Sichuan rainstorm influenced by terrain. *Chinese J. Atmos. Sci.*, **37**(5), 1099–1110. (in Chinese)

Wang, W., J. Liu, and X. J. Cai, 2011: Impact of mesoscale gravity waves on a heavy rainfall event in the east side of the Tibetan Plateau. *Transactions of Atmospheric Sciences*, **34**(6), 737–747. (in Chinese)